CHEMISTRY
A EUROPEAN JOURNAL

DOI: 10.1002/chem.200501019

Calcite Mesocrystals: “Morphing” Crystals by a Polyelectrolyte

Tongxin Wang, Markus Antonietti, and Helmut Cölfen*[a]

Abstract: Crystallization of calcite from different concentrated calcium chloride solutions by the CO_2 vapor diffusion technique in the presence of polystyrenesulfonate (PSS) yields defined assemblies of nanoparticles with unusual morphology. From the typical calcite rhombohedra, the morphology can be systematically varied via rounded edges and truncated triangles to concavely bent lens-like shapes. Although these “crystals” are apparently well facetted as observed in light microscopy, electron microscopy analysis and BET isotherms reveal that the structures are highly porous and are composed of almost perfectly three-dimensionally aligned calcite nanocrystals, scaffolded to the final, partly curved structures. The formation of all mesostructures is discussed within the framework of a polymer-mediated structure-formation process, in which the polymer is acting in four different ways. The present model case also provides evidence for the importance of nonclassical mesoscopic processes in polymer-controlled crystallization in general.

Keywords: biomineralization • crystallization assembly • mesocrystals • morphosynthesis • polymers

Introduction

The control of crystallization processes is one of the most important techniques in the preparation, purification, and application of solid substances. Control of crystal size and shape ensures desired dissolution rates (e.g. of pharmaceuticals), and control of crystal shape and texture defines flow properties, space filling by the powder, and mechanical properties. High reproducibility of the chosen procedures ensures the quality of industrial products and is of utmost importance, as easily elucidated in the case of calcium carbonate abrasives and filler particles. As nucleation and growth are very sensitive processes, crystallization is usually controlled by addition of nucleation agents, stabilizers or ternary components in general. The choice of solvents,[1] low molecular additives, surfactants and functional polymers is regularly reported (for recent reviews, see references [2–5]).

In addition to nucleation and growth control, it was recently revealed that there is also a nonclassical pathway of crystallization via colloidal intermediates and mesoscale transformation.[6–8] The evidence for this process was also recently reviewed.[3,9] On this pathway, crystalline structures are constructed by assembly and/or transformation from larger units (instead of by addition of single ions). For example, both Addadi and Weiner[10], and Cölfen and Mann[3] independently reviewed the role of amorphous nanoparticles in bio- and biomimetic mineralization. The role of similar intermediates in $CaCO_3$ scale formation, as well as their experimental identification, is also a question of larger industrial relevance.[11,12] Taden et al. analyzed a model system constituted of dye nanodroplets, which formed highly ordered dye crystals of unexpected size by mesoscale transformation.[8] Mesoscale assembly and transformation also appears to take place for inorganic crystalline solids such as iron oxides,[13] cerium oxide,[14] copper oxalate,[6] and copper oxide.[15]

The addition of an interacting polymer to the crystallization solution can modify the ongoing processes in various different ways (Figure 1):

- first, by complexing the ions, the polymer can block or retard the growth path of single ions, making assembly effects (**b, c**) more significant then the classical crystallization route (**a**)
- it can act as a nucleation agent by lowering the interface energy of subcritical and critical nuclei, increasing the number of primary nanoparticles (**e**)
- it can colloidally stabilize metastable intermediates, such as amorphous precursor structures (**c**)

---

[a] Dr. T. X. Wang, Prof. Dr. M. Antonietti, Dr. H. Cölfen
Max Planck Institute of Colloids and Interfaces
Department of Colloid Chemistry
Research Campus Golm, 14424 Potsdam (Germany)
Fax: (+49) 331-567-9502
E-mail: coelfen@mpikg.mpg.de

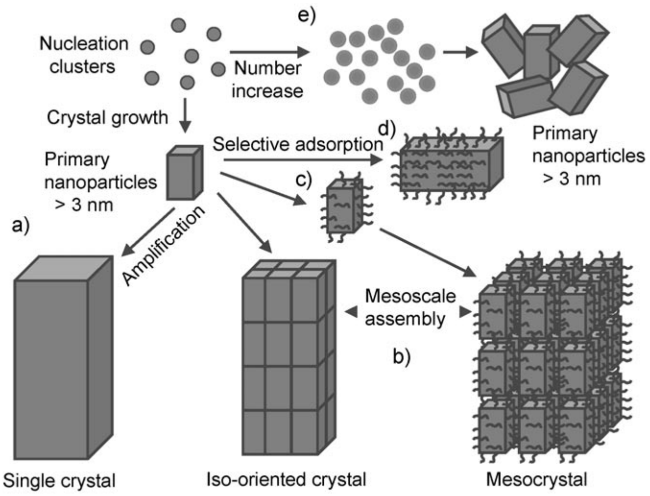

Figure 1. Crystallization by addition of ions (slow, a) or mesoscale aggregation and alignment (fast, b), partially adapted from reference [3]. Crystallization control by particle stabilization (c), crystal shape changes by selective polymer adsorption (d) or changes of primary nanoparticles (e) is also shown.

- it can alter the shape of the primary nanoparticles by selective adsorption and/or enrichment onto specific crystal faces (**d**), which leads to growth inhibition of these crystal faces.[16]

Additionally, the polymers can induce aggregation through a change in colloidal stability (for instance, by depletion[17,18]) or modified interaction potentials, where crystal alignment can occur in a directed fashion.

Usually, the added polymers adopt more than one, if not all roles mentioned in the list, which makes a prediction of crystal morphology impossible. This is in contrast to the idealized thermodynamic description, which has been proposed early last century by Wulff.[19]

If the polymer is tightly bound to the particles, the primary hybrid particles are organized into a mesoscopic superstructure by the anisotropy of their shape, specific steric, electrostatic, van-der-Waals and hydrophilic–hydrophobic interactions.

Organization of nanocrystals in crystallographic registers to defined microstructures with more or less defined external faces takes place.[9,20] Such “mesocrystals” have already been described for calcium carbonate systems,[21,22] $BaSO_4$,[23] copper oxalate,[6] CdS,[24] $CoPt_3$,[25] and D,L- alanine,[20,26] and many others, as reviewed in reference [9]. The reasons for the almost perfect alignment of the mesoscopic building units with respect to each other are currently explored, and long-range interactions are certainly involved.

$CaCO_3$ is a scientifically and industrially important mineral system, and its crystallization control has attracted extensive attention for decades, as reviewed recently.[27,28] Until now, a whole variety of additives or templates such as biomacromolecules,[29–34] synthetic polymers,[5,28,35–37] low molecular weight compounds,[38–40] solid matrices[41,42] as well as Langmuir monolayers,[43–45] or self-assembled films,[46,47] were effectively used to control $CaCO_3$ morphologies and polymorphs.

In a recent communication, we presented a very simple model system composed of calcite and PSS.[48] A remarkable change from the typical single crystal calcite rhombohedra with {104} faces to mesocrystals presenting the unusual {001} faces was found. It is the task of the present paper to extend these primary observations on the calcite/PSS mesocrystal system, where, by appropriate adjustment of concentrations, the mesomorphology will be varied over a broad range in a systematic fashion. Thus, we hope to answer the question of how the polymer interferes with the crystallization and aggregation process in more detail.

Experimental Section

The following chemicals were purchased and used without further purification: $CaCl_2{\cdot}2H_2O$ (Fluka, $\geq 99\,\%$), poly(sodium 4-styrenesulfonate) (PSS, $M_w \approx 70000\,\mathrm{g\,mol^{-1}}$) (Aldrich). Double-distilled water was used for the preparation of the crystallization solutions.

Crystallization of $CaCO_3$: The mineralization was performed by a slow CO_2 gas diffusion technique described by Addadi et al.[33] To compare the effect of polymer and calcium, crystallizations in the presence of different concentrations of PSS and $CaCl_2$ were carried out in glass bottles with glass slides, which were kept in a closed desiccator at room temperature. All glassware was cleaned as follows: firstly sonicated in ethanol, then rinsed with distilled water, further immersed in a H_2O–HNO_3-(65 %)–H_2O_2 (1:1:1, v/v/v) solution, then rinsed with double-distilled H_2O, and finally dried at room temperature.

A stock solution of $CaCl_2$ (10 mM) was freshly prepared in boiled double-distilled water through which N_2 was bubbled overnight. From this stock solution, 5-mL solutions with different concentrations of polystyrenesulfonate (1, 0.5, 0.1 $\mathrm{g\,L^{-1}}$) and $CaCl_2$ (5, 2.5, 1.25 $\mathrm{mmol\,L^{-1}}$) were prepared under vigorous stirring. The solutions were distributed into different glass bottles with a glass slide on the bottom (1 mL solution in each bottle) for further crystallization experiments. The bottles were covered with Parafilm, three needle holes were punched into the film, and the bottles were placed in a larger desiccator. Two small glass bottles (10 mL) with crushed ammonium carbonate were also covered with Parafilm, three needle holes were punched into the film, and the bottles were placed at the bottom of the desiccator as the source of CO_2. At different times, the bottles with the crystals were removed from the desiccator, the glass slides carrying the crystals were separated from the solution, rinsed shortly with distilled water and directly examined by optical microscopy. Scanning electron microscopy (SEM) and other techniques were performed on the crystals after they had been dried at room temperature.

Analytical methods: Optical microscopy and SEM were applied to all samples. The use of light microscopy as technique is necessary to show that the SEM images are free of drying artefacts that may result from the sample preparation. In addition, polarized light microscopy allows the identification of the calcite *c* axis, which is the only direction free of birefringence. The SEM measurements were performed on a LEO 1550 - GEMINI. Transmission electron microscopy (TEM) as well as electron diffraction were performed on a Zeiss EM 912 Omega microscope at 120 kV with a 580-mm camera. Light microscopy images of samples in solution were taken with an Olympus BX50 or BX41 microscope connected to a MONACOR TVCCD-460 color camera. Powder X-ray diffraction (XRD) patterns were recorded on a PDS 120 diffractometer (Nonius GmbH, Solingen) with $Cu_{K\alpha}$ radiation. Thermogravimetric analyses were performed on a Netzsch TG 209, and the samples were examined under an oxygen atmosphere at a scanning rate of $20\,\mathrm{K\,min^{-1}}$ from room temperature to 800 °C. The surface cleavage of the crystal faces, the unit cell structure, and the modeling of morphologies were performed with the Cerius^2 software (Accelrys).

Dynamic light scattering (DLS) measurements were carried out using a standard, laboratory-built scattering spectrometer operating at 633 nm (argon-ion laser, Coherent, Model Innova 300) (power: 30–600 mW) at scattering angles of 90°. The radius distribution of the particles in solution was calculated from the experimental correlation functions using the program FASTORT.exe.[49] Samples for DLS were freshly prepared in 5 mL aqueous solution. BET sorption measurements were carried out on 1 mg of sample at 77 K using an Autosorb-1 from Quantachrome Instruments. Desorption curves are not used due to hysteresis effects.

Results and Discussion

Calcium carbonate crystallizes within the presented crystallization setup and procedure in the absence of additives in one day into calcite rhombohedra (data not shown). The addition of minor amounts (0.1 $g L^{-1}$) of polystyrenesulfonate (PSS) led to two effects. On the one hand, all the crystalline species became very homogeneous in morphology and size. This is easily explained by a better control of nucleation by PSS. The improved nucleation is also reflected by the increasing number and decreasing size of $CaCO_3$ particles with increasing PSS concentration (data not shown). Time-resolved microscopic studies showed an increasing number of crystals within the first 10 h, without obvious size and shape changes. This indicates a continuous nucleation of $CaCO_3$ crystals in the early crystallization stages.[50]

On the other hand, with PSS addition, the surface structure of the formed crystalline superstructures increased in roughness, and selected corners/edges became rounded. All of the described crystal morphologies are very stable, once formed. A typical result of high-resolution scanning electron microscopy (HRSEM) of the obtained particles is shown in Figure 2.

The formation of porous crystals, rough surfaces, and rounded corners are very strong indications for the alteration of the crystallization mechanism from ionic growth to mesoscale assembly.[23] PSS, as a polyelectrolyte, strongly binds free Ca^{2+} ions,[51] decreases the free Ca^{2+} ion concentration by intermediary binding, and thus slows down the related speed of growth by addition of single ions. We propose that this PSS–Ca complex is the primary species. With increasing carbonate concentration, the better-binding carbonate ions compete with the sulfate ions for the highly localized and enriched Ca^{2+} ions close to the PSS backbone, presumably initially forming a mixed nanoparticle composed of hydrated, amorphous $CaCO_3$ and PSS.

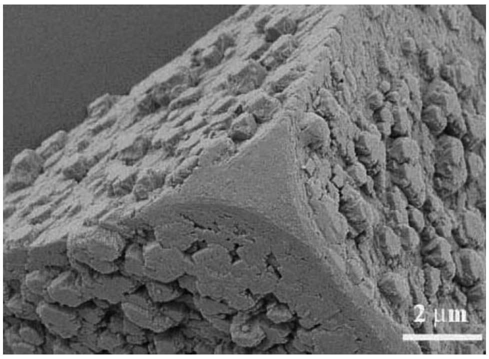

Figure 2. High-resolution SEM image of a crystal obtained from 1 mL of 1.25 $mmol L^{-1}$ Ca^{2+} solution with 0.1 $g L^{-1}$ (PSS). Samples were obtained on a glass slip by a gas diffusion experiment after one day. Note the formation of rounded corners.

The existence of such colloidal PSS–Ca complexes and amorphous intermediates can be proven with analytical solution techniques. Time-dependent dynamic light scattering (DLS) on the whole investigated range of samples reveals the existence of nanoparticles in solution already well ahead of crystallization, and TEM, in conjunction with electron diffraction, shows that the early nanoparticles are amorphous.[48] This was independently confirmed by the so-called density variation method in analytical ultracentrifugation.[52] It was revealed that the density of all investigated precursor particles is between 1.44 and 1.58 $g mL^{-1}$, in agreement with the amorphous $CaCO_3$ density of 1.49 $g mL^{-1}$ determined by small-angle X-ray scattering by Ballauff et al.[53]

The $CaCO_3$ nanocrystals are presumably nucleated from these mixed amorphous species, with the PSS then immediately associated nearby. This mechanism provides the large number of fine, metastable crystals needed for mesoscale assembly.

Nitrogen sorption measurements evaluated according to Brunauer–Emmett–Teller (BET, Supporting Information Figure S1) on the final dried structures show that the formed calcite mesocrystals are highly porous, with specific surface areas for three different species always larger than 260 $m^2 g^{-1}$. The size distribution curves calculated from the adsorption branch of nitrogen isotherms show that the pores are in the mesopore range, with maximum pore diameters of approximately 3–10 nm, depending on the system. This goes well with a primary crystal size of approximately 30 nm and an interstitial channel system between the primary crystallites. Pore volumes of the samples were calculated to be in the range of 0.26–0.51 $mL g^{-1}$, using the Brunauer, Joyner & Halenda theory under the simplifying assumption of cylindrical pores.

Approximately 50-nm-sized tectonic elements were detected on the mesocrystal surface by AFM (data not shown). These results also clearly exclude crystal growth by Ostwald ripening, which would lead to a fused single crystal without any pores. AFM also shows that the mesocrystal generation is accompanied by numerous defect structures on the nanoscale, despite the external facetted morphology being well-defined.

The concentration of PSS has a very strong influence on the morphology of the crystalline superstructures in the otherwise standardized crystallization process. This is depicted in Figure 3, in which both the Ca^{2+} as well as the PSS concentration was varied in a systematic fashion.

The case presumably closest to classical crystallization is the one with the lowest Ca^{2+} concentration of 1.25 $mmol L^{-1}$ combined with the lowest polyelectrolyte concentration of

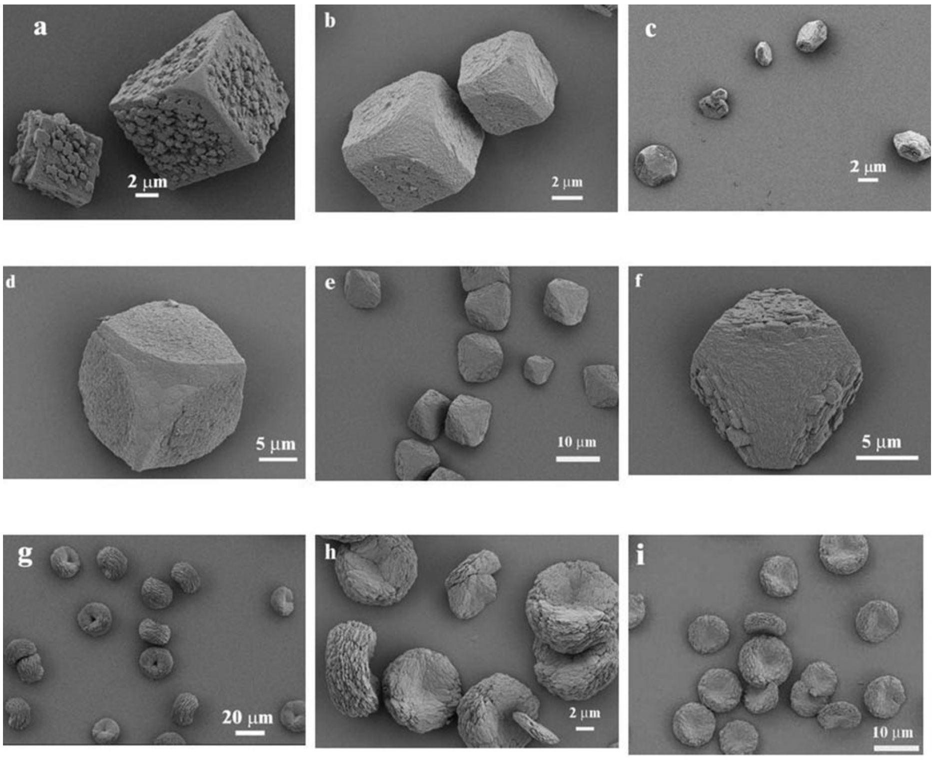

Figure 3. Typical SEM images of calcite mesocrystals obtained on a glass slip by the gas diffusion reaction after 1 day in 1 mL of solution with different concentrations of Ca^{2+} and polystyrenesulfonate: a) $[Ca^{2+}]=1.25\ mmol\,L^{-1}$, $[PSS]=0.1\ g\,L^{-1}$; b) $[Ca^{2+}]=1.25\ mmol\,L^{-1}$, $[PSS]=0.5\ g\,L^{-1}$; c) $[Ca^{2+}]=1.25\ mmol\,L^{-1}$, $[PSS]=1.0\ g\,L^{-1}$; d) $[Ca^{2+}]=2.5\ mmol\,L^{-1}$, $[PSS]=0.1\ g\,L^{-1}$; e) $[Ca^{2+}]=2.5\ mmol\,L^{-1}$, $[PSS]=0.5\ g\,L^{-1}$; f) $[Ca^{2+}]=2.5\ mmol\,L^{-1}$, $[PSS]=1.0\ g\,L^{-1}$; g) $[Ca^{2+}]=5\ mmol\,L^{-1}$, $[PSS]=0.1\ g\,L^{-1}$; h) $[Ca^{2+}]=5\ mmol\,L^{-1}$, $[PSS]=0.5\ g\,L^{-1}$; i) $[Ca^{2+}]=5\ mmol\,L^{-1}$, $[PSS]=1.0\ g\,L^{-1}$.

$0.1\ g\,L^{-1}$ (Figure 3a). Low concentrations are also coupled to lower supersaturation and slower growth. At this concentration couple, rhombohedral calcite structures are still found, however obviously composed of smaller calcite subcrystals. The mesocrystal still exposes the six {104} faces, showing that the influence of the polymer on the mutual alignment is still weak. Note, however, that these species already possess two rounded corners in the (001) direction (see also Figure 2). Interestingly and indicating generality, similar structures with rounded corners and rough surfaces were described before.[54,55] Single-crystal analysis could be used to index their outer faces.[22,55]

If the PSS concentration is increased to $0.5\ g\,L^{-1}$ at a fixed low Ca^{2+} concentration of $1.25\ mmol\,L^{-1}$ (Figure 3b), a finer texture of the primary nanoparticulate building blocks is found. This underlines our view that the primary units are nucleated in the proximity of the polyelectrolyte, as more polyelectrolyte can then nucleate a larger number of particles. The two "rounded" corners along the (001) direction (where 1 is at the back of the crystals in Figure 3b) are more pronounced. This suggests that the efficiency of aggregation of the primary particles is lowered in direction of the *c* axis. As this is the only nonbirefringent orientation of calcite, the orientation can be easily assigned by polarized light microscopy (Figure S2e, f in the Supporting Information). Furthermore, six out of the eight edges are rounded. It is worth mentioning that this morphology, with minor modifications, reoccurs for two other concentration pairs, also at higher calcium concentrations in the morphology map, see Figure 3d and Figure 3e. It seems to be a generic structure, and the finer the surface textures at higher Ca^{2+} (or higher polymer) concentrations are, the more pronounced the rounding of the two corners in the *c* direction is. The discrimination of the *c* axis allows a more detailed understanding of the mesoscale assembly process. The *c* axis of calcite has hexagonal symmetry and is usually not exposed, as it is constituted by either pure cationic or anionic sites. The corresponding Cerius^2 representation of this face is shown in Figure 4.

It is easy to understand why this surface is specifically stabilized by the PSS: the multiple cationic sites can bind the negative polyelectrolyte, and by this binding a low-energy surface is obtained. We assume that this surface structure originates from a PSS–Ca complex precursor, that is, the inherent Ca^{2+}-rich character of the crystal face and the PSS charge counterbalance is predefined in the precursor. The involved multiple binding of a polyelectrolyte onto the (001) surface also explains the very high binding efficiency and stability of the nanoparticle assembly at comparably low concentrations.

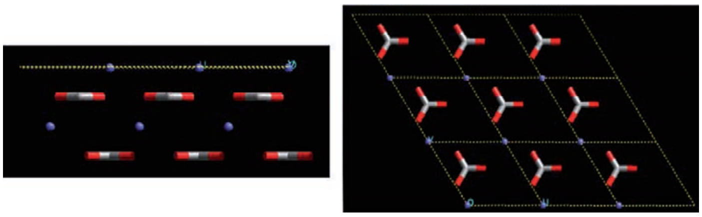

Figure 4. Cerius^2 presentation of the calcite (001) surface, which is indicated by the yellow dashed line. Ca^{2+} blue, C gray, O red. Left: Side view, Right: Top view of a 3×3×2 unit-cell arrangement; the hexagonal symmetry of this face is clearly visible.

Increasing the polyelectrolyte concentration to $1\ g\,L^{-1}$ (the maximum applied concentration) at a still low Ca^{2+} concentration of $1.25\ mmol\,L^{-1}$ leads to a new, but related

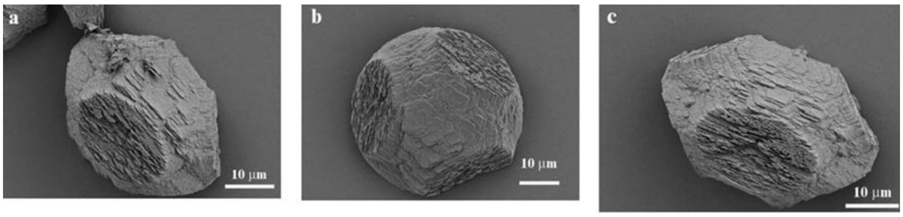

Figure 5. Typical SEM images of calcite mesocrystals (the same sample as Figure 3c) obtained on a glass slip by the gas diffusion reaction after 1 day in 1 mL of solution with 1.25 mmolL^{-1} of Ca^{2+} and 1.0 gL^{-1} of PSS.

morphology, presented in Figure 3c and—in more detail—in Figure 5.

The suppression of nanoparticle assembly along the six edges and two corners has progressed so far that the whole structure has no similarity to the primary rhombohedron anymore. The missing edges overlap to an extent that the whole structure is partly rounded, leaving six elliptical side faces. The architectural program to set up this complicated superstructure of flat and curved planes is nevertheless quite precisely kept throughout the sample, as seen by the comparison of three different, randomly chosen particles from different viewing angles (Figure 5). From the finer details of these HRSEM pictures, it becomes obvious that the whole structure is composed of hexagonal/truncated trigonal plates of calcite, which again expose the unusual (001) face. The six removed edge directions are clearly not planar or even faces in a classical sense, and thus cannot be explained by the classical picture of polyelectrolyte adsorption to stabilize faces of a single crystal. Although crystalline with respect to the primary nanoparticle building units, the mesocrystals are strongly curved. Active shaping in these directions is driven by lowered efficiency of assembly and stacking.

As these mesocrystals are unusually rough, higher resolution SEM pictures (Figure 6) reveal additional information on the assembly process. Within the disordered pore structure one can identify primary, roughly globular nanoparticles, approximately 30 nm in size, which assemble in a first integration step towards 100–300 nm thick plates. These plates are, however, astonishingly disordered on the mesoscale. The single plates are obviously not connected, or just weakly intergrown, which indicates incorporation of the polyelectrolyte into the structure. This is also supported by the thermogravimetric analysis (TGA) of these structures, which hints at a relative polymer content of approximately 3 wt%. However, the vectorial alignment between the single plates seems to be close to perfect, which results in excellent order on the micrometer range which is much higher than the order on the mesoscale.

When keeping the polymer concentration high (1.0 gL^{-1}) and increasing the Ca^{2+} concentration (2.5 mmolL^{-1}), the next, related morphology develops (Figure 3f). The exposure of the (001) and (00−1) faces has increased in a way that the whole sample now adopts a truncated trigonal morphology (Figure 7).

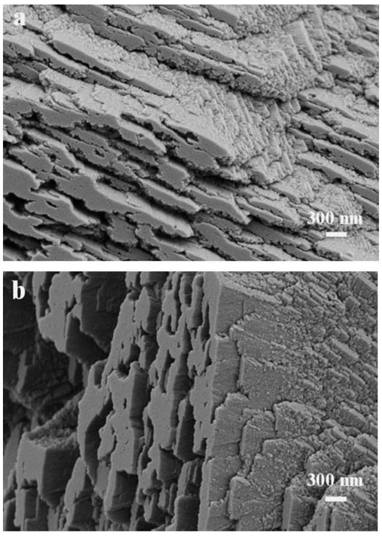

Figure 6. High-resolution SEM images of calcite mesocrystals (the same sample as Figure 3c) obtained on a glass slip by the gas diffusion reaction after 1 day in 1 mL of solution at 1.25 mmolL^{-1} of Ca^{2+} and 1.0 gL^{-1} of PSS.

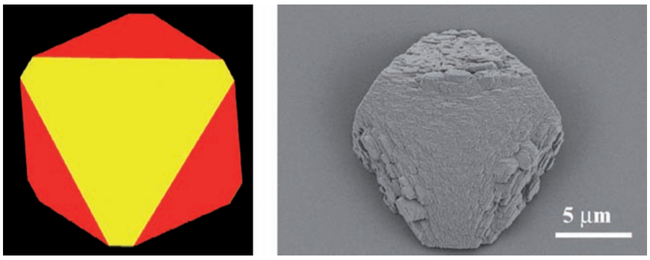

Figure 7. Left: Cerius^2 color model of truncated trigonal calcite structure view of the 001 face (yellow) and the 104 face (red). Right: The corresponding assembly motif, according to Figure 3f.

The two dominant (001) faces are now connected with the remainders of the six (104) faces, which is the minimal surface-area construction to connect the two (001) faces. It was already mentioned that the (001) direction, due to its symmetry, is the only axis in calcite which is not birefringent. Consequently, those crystals are black in the polarization microscope when looking upon the (001) faces, whereas all other faces are bright (see Figure S2 in the Supporting Information). Interestingly, there is an analogous case of morphology control in biomineralization:[56] the eye lens of five-hundred-million-year old trilobites is also made of hexagonal calcite oriented towards the unusual [001] direction in a very similar fashion, as this is the only direction where clear sight (without double vision) can be obtained.

The most complicated structure series is obtained at highest Ca^{2+} concentrations of 5 mmolL^{-1}; see Figure 3g–i. Semiconvex–concave crystalline assemblies are formed, which are only weakly dependent on polymer concentration. The formation does not depend on the relative concentration of Ca^{2+} to PSS, as similar ratios for other Ca^{2+} concentrations resulted in other structures (Figure 3). Indeed, it is the high Ca^{2+} supersaturation which leads to the exotic morphology. The assemblies, as shown in higher resolution in Figure 8, are roughly circular in the [001] direction (as seen by the typical truncated-trigonal in-plane texturation), but show a convex/concave discrimination of the two perpendicular sides.

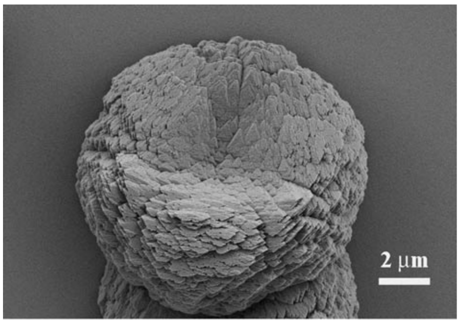

Figure 8. Typical convex–concave structure of calcite at high Ca^{2+} concentration (5 mmolL^{-1}). The sample was obtained on a glass slip by the gas diffusion reaction after 1 day in 1 mL of solution with 0.5 gL^{-1} of PSS.

A time-dependent SEM study revealed that there is a morphology change throughout particle growth (see Figure S3 in the Supporting Information): at the early stage after 3 h, biconvex particles approximately 600 nm in size are formed, which develop the convex–concave morphology upon further growth. This is indicative of continued nanoparticle attachment to an existing, initially symmetric particle, which however has different surface properties on the two opposite sides.

The lower the polymer concentration, the more pronounced the asymmetry and the more bent the structures are, until a central hole on one side is finally formed. This morphology is contradictive to all classical pictures of crystallization, for which such a hole should immediately vanish by Ostwald ripening, and where symmetry is encoded in the primary unit cells and thermodynamics, as described by the Wulff-law of crystal growth.[19]

Such a hole (= no effective mass transport) with a pile (= increased effective mass transport) on the opposite side strongly indicates dipolar long-range interactions controlling the growth and mesoscale assembly of such structures. Wulff's law only considers short-range interface energies (i.e. energies in the plane) as the driving force, but inclusion of long-range energy contributions might indeed explain the different mesocrystal morphologies. A model case of such long-range interactions is the presence of a dipolar field, as already proposed by Kniep et al. for the rod–dumbbell–sphere transition described for fluoroapatite crystallization in gelatin gels.[57,58]

Owing to the simplicity of the present system and the possibility to experimentally assign the (001) face, a model for the generation of a dipole moment in the otherwise nondipolar calcite structure can be given (Figure 9).

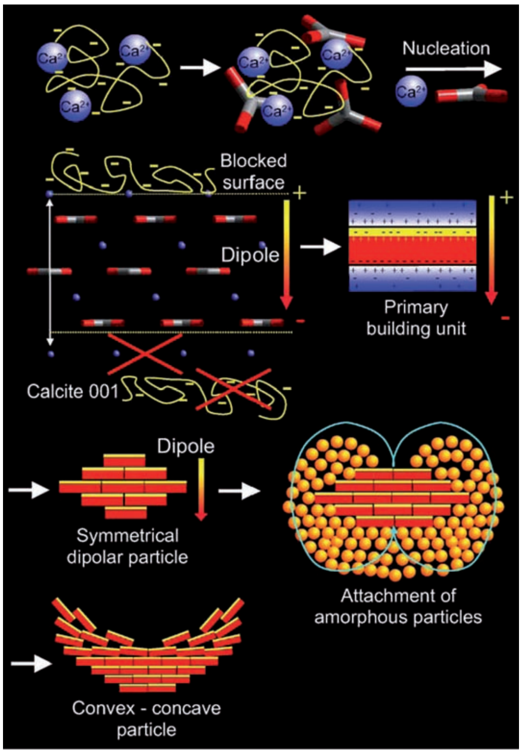

Figure 9. Mechanism of the final morphology change in calcite crystals due to selective adsorption of PSS to one (001) face and the resulting build up of an inner dipole moment within the crystal along the *c* direction. The primary crystals are asymmetric as they bind the polymer only on one side. These primary blocks assemble to give flat, pseudo-symmetric mesocrystal structures. When a certain size is exceeded, not only primary platelets, but also amorphous intermediates are attracted. By recrystallization of those species, bent crystalline structures without translational order can develop.

The very high Ca^{2+} supersaturation results in fast nucleation of very small, thin platelets. The highly positive, pure Ca- exposing (001) face is ideal for the adsorption of PSS, making this face energetically very favorable and exposed. Once the crystal has nucleated in this direction from the precursor, the polymer will effectively block this face from further growth. The counterface, at least for nanosized platelet crystals, now has to be a CO_3^{2-} ion-terminated (001) face, as two positive planes in such proximity (smaller than ca. 40 nm) would repel each other throughout the crystal. As a result, no further carbonate or PSS layer can adsorb on this counterface, as this is charge-forbidden.

As the primary platelet (Figure 9, red) carries the polyelectrolyte on one side (Figure 9, yellow), but is negatively charged on the counterface as well, such a structure is colloidally stable with respect to direct charge interactions and carries the typical electrostatic double layer (Figure 9, blue). However, such an asymmetric stacked structure always comes with a strong dipole moment, brought in by the two oppositely charged crystal splitting planes. Note that the dipole moment is dependent on the thickness of the crystal, that is, the double layer (2-nm thick; under the applied conditions) cannot compensate for the charge separation over the platelet (ca. 40 nm thick; see Figure S4 in the Supporting Information).

This simple argument reveals a new possible source of dipolar fields associated with highly symmetric ionic nanocrystals, which are otherwise nonpolar on the basis of their crystal symmetry. Previous reports in the literature have focused on the specific binding of a polymer to a distinct crystal surface[5] or surface dipole fields ranging into the solution,[57,58] which however are known to be weak and screened by the ionic strength of the solution. Our view is based on the natural dissymmetry of a nanocrystal with highly charged planes, with the surface-charge-generated electric field being strong and long-ranged throughout the crystal. It is important to repeat that ionic crystals possess a rather low dielectric constant (usually $\varepsilon \approx 5$), and that the nonscreened Coulomb law holds within the structure (instead of the screened Coulomb law in solution). Therefore, electric fields are much stronger and more long-ranged throughout a nanocrystal than through the aqueous environment.

In essence, a calcite nanocrystal with the cationic (001) face stabilized by an anionic polyelectrolyte will generate an anionic counter side. This counter side cannot grow by addition of single ions, as anions are repelled by charge repulsion from the surface, and cations cannot add to the crystal because of the inner field effects (Figure 9). The whole structure can then only grow by assembly of other neutral species, either by addition of ion pairs (rare) or by aggregation with another completed, dipolar crystalline slab (the actual case).

For high Ca^{2+} supersaturations, a rough estimate of the single platelet thickness on the basis of the HRSEM data (see Figure S4 in the Supporting Information) gives approximately 40 nm. A simple calculation based on Coulomb's law shows that the field strength on the other side of the crystal is of the order of some hundred kT (thermal energy). The resulting nanoplatelets possess a dipole moment perpendicular to the plane, based on the different surface structures. Such dipolar platelets will align in three dimensions to minimize their mutual interaction energy, and in that way promoting the build-up of an even larger dipole moment in the growing stack.

Above a critical size, due to the linear dependence of the dipole moment on thickness, a new effect sets in. The inner dipole moment is getting so large that not only the dipolar nanoplatelets (as for the first set of morphologies), but also polymer-stabilized amorphous intermediates are attracted. As these small particles have, owing to the polyelectrolyte component, a homogeneous surface charge of one type (presumably negative), the potential of the attracting amorphous intermediates defines the moment where the mesostructures develop curvature and dissymmetry: the one, similarly charged pole in the middle of one mesocrystal (001) face repels all intermediates from further crystal growth (and a hole is formed), whereas the other oppositely charged pole attracts the particles. As there is a continuous change from attractive to repulsive interaction from pole to pole, the continuous variation of aggregation probability leads to the finally observed, nicely curved concave/convex particle morphology. The existence of strong dipole fields in the final mesostructure is also proven by their non-statistical overall orientation on the substrate: We were not able to find a single mesostructure (out of several thousands) of this type which was positioned with the hole or cavity towards the (usually negatively charged) substrate.

A question that remains unresolved by this model is why the single platelets put themselves into crystallographic register, that is, why do they also vectorially align in the two other, in-plane directions. We can only speculate that the single platelets in close proximity are able to detect their epitactic, complementary hexagonal charge patterns throughout the layer of polystyrenesulfonate.

Additional experimental evidence for the organization scheme of the convex–concave assembly structure was obtained by polarization light microscopy (see Figure S2a, b in the Supporting Information), where the images show a dark spot in the center of the structures, indicative of the calcite (001) orientation. Time-dependent experiments (see Figure S5 in the Supporting Information) show that the principal (001) orientation of the growing mesostructures is kept throughout the whole process of crystallization, although the structure develops the bent rims without register into the *c* axis at the end of the crystallization process.

In a recent investigation the truncated calcite morphology, as shown in Figure 3 f and Figure 7, was also reported.[59] These crystals were, interestingly enough, obtained by adsorption of methylene blue containing a sulfonate group, similar to the PSS molecules used in this study. A final proof of the dipolar character of the convex–concave mesocrystals therefore can be obtained by staining experiments with charged dyes. If a positively charged dye (fast dark blue) is added to the final convex- concave crystals, only the top is stained (see Figure S6 in the Supporting Material), whereas the addition of a negatively charged dye (Congo red) selectively stains the sides of the mesocrystals.

We think that the observations of the present, comparably simple system can be generalized and explain a vast variety of unusual observations described in the crystallization literature. Asymmetry of face and counterface is presumably an inherent feature of most crystallization processes controlled by charged additives, as long as the building blocks are on the nanoscale, and the dipolar growth patterns found by Kniep et al.,[57,58] or the piezoelectricity of bone[60] made from otherwise nondipolar, mirror-symmetric hydroxy/fluoroapatite can—alternatively to the current explanation—also be promoted by the formation of dipolar poled mesocrystal aggregates at the beginning of structure formation.

Similar effects are found in the polymer-controlled crystallization of $CaCO_3$[61] or $BaCO_3$ and other heavy-metal carbonates.[62]

The attraction/repulsion of the two opposite faces through the crystal in addition explains the existence of the universally observed characteristic length of the order of some tens of nanometers in additive-controlled nanocrystal growth, as for instance the constant thickness of nanofibers[63–65] or nanoplates.[66] A certain thickness of 10–100 nm is indeed needed, depending on the crystal/additive pair, until the two opposite sides can be indeed equal with respect to their surface charge, also allowing additive adsorption on both sides. Below this thickness, the electrostatic forces within the growing crystal restrict addition of materials up to a critical crystal thickness.

Conclusion

The slow crystallization of calcite by the gas diffusion technique results in the presence of the negatively charged, Ca-binding PSS yields, depending on the relative Ca^{2+} and PSS^- concentration in a family of well-defined crystalline mesostructures or mesocrystals, that is, regular scaffolds composed of separated, but almost perfectly three-dimensionally aligned calcite nanocrystals. Using HRSEM and following the development of the structures as a function of the reactant concentrations, it was possible to reveal the inner architecture principles of these mesocrystals. The observed systematic behavior can only be explained by the polymer interacting with the crystallization process in a variety of modes: First, it strongly binds free calcium ions and shifts the mechanism from ionic growth in the default experiment without additive to mesoscale assembly of preformed nanoblocks in presence of the polymer.

In addition, the polymer acts as a nucleation agent, as revealed by polymer concentration variation. Over wide regions of the morphology map, increase of polymer concentration and increase of Ca^{2+} supersaturation seem to have a similar influence, indicating that the nanoparticles nucleate from a carbonized PSS–Ca complex. The primary building units of the mesocrystals are amorphous nanoparticles, which crystallize to calcite as revealed by WAXS and DLS. In addition, PSS seems to bind quite selectively to the otherwise nonexposed (001) face of calcite, favoring mesostructures composed of truncated triangular units instead of rhombohedra.

For high supersaturations and correspondingly small primary particles, a new effect appears as the system obviously changes and looses long-range translational symmetry in favor of a dipolar arrangement of primary nanoparticles. It was reasoned that spontaneous asymmetry might be characteristic for very small particles stabilized by charged polymers, as inner-field effects within the crystal cannot be neglected on smaller scales. This model also explains the spontaneous occurrence of dipole effects in materials with nondipolar unit cells, such as dumbbell-like growth patterns of crystals or piezoelectricity in the growth direction. Obviously, such mesocrystals grown from polymer-protected nanocrystals can exhibit dipolarity based on the asymmetry of splitting planes with opposite surface charge, whereas single crystals of the same material cannot. Future work will address the importance of electric fields on structure formation by performing similar processes in external electric fields and in the presence of salts. In addition, other mechanisms to control crystal self-assembly will also be investigated to fully reveal the design principles of these fascinating crystalline superstructures.

Acknowledgements

We thank the Max Planck Society for financial support and a fellowship for T.X.W. The authors also thank Antje Völkel for AUC, Dr. Andreas Erbe for DLS, Torsten Brezesinski for BET, Dr. Jürgen Hartmann for TEM and SAED, Dr. Zhixiang Wei for TGA and WAXS measurements. Dr. Bernd Smarsly and Dr. Charl Faul are thanked for their helpful discussions.

---

[1] M. Lahav, L. Leiserowitz, *Chem. Eng. Sci.* **2001**, *56*, 2245–2253.
[2] L. A. Estroff, A. D. Hamilton, *Chem. Mater.* **2001**, *13*, 3227–3235.
[3] H. Cölfen, S. Mann, *Angew. Chem.* **2003**, *115*, 2452–2468; *Angew. Chem. Int. Ed.* **2003**, *42*, 2350–2365.
[4] F. C. Meldrum, *Int. Mater. Rev.* **2003**, *48*, 187–224.
[5] S. H. Yu, H. Cölfen, *J. Mater. Chem.* **2004**, *14*, 2124–2147.
[6] N. Jongen, P. Bowen, J. Lemaître, J. C. Valmalette, H. Hofmann, *J. Colloid Interface Sci.* **2000**, *226*, 189–198.
[7] R. L. Penn, J. F. Banfield, *Geochim. Cosmochim. Acta* **1999**, *63*, 1549–1557.
[8] A. Taden, K. Landfester, M. Antonietti, *Langmuir* **2004**, *20*, 957–961.
[9] H. Cölfen, M. Antonietti, *Angew. Chem.* **2005**, *117*, 5714–5730; *Angew. Chem. Int. Ed.* **2005**, 44, 5576–5591.
[10] L. Addadi, S. Raz, S. Weiner, *Adv. Mater.* **2003**, *15*, 959–970.
[11] D. Horn, J. Rieger, *Angew. Chem.* **2001**, *13*, 4460–4492; *Angew. Chem. Int. Ed.* **2001**, *40*, 4330–4361.
[12] J. Rieger, *Tenside Surfactants Deterg.* **2002**, *39*, 221–225.
[13] E. Matijevic, P. Sheiner, *J. Colloid Interface Sci.* **1978**, *63*, 509–524.
[14] W. P. Hsu, L. Ronnquist, E. Matijevic, *Langmuir* **1988**, *4*, 31–37.
[15] S. H. Lee, Y. S. Her, E. Matijevic, *J. Colloid Interface Sci.* **1997**, *186*, 193–202.
[16] J. H. Adair, E. Suvaci, *Curr. Opin. Colloid Interface Sci.* **2000**, *5*, 160–167.
[17] B. Vincent, *The Stability of Solid/Liquid Dispersions in the Presence of Polymers in Solid/Liquid Dispersions* (Ed.:T. F. Tadros), Academic Press, London, **1987**.
[18] G. J. Fleer, M. H. Cohen Stuart, J. M. H. Scheutjens, T. Cosgrove, B. Vincent, *Polymers at Interfaces*, Chapmann Hall, **1993**.
[19] G. Wulff, *Z. Kristallogr.* **1901**, *34*, 449–480.
[20] S. Wohlrab, N. Pinna, M. Antonietti, H. Cölfen, *Chem. Eur. J.* **2005**, *11*, 2903–2913.
[21] J. H. Zhan, H, P. Lin, C. Y. Mou, *Adv. Mater.* **2003**, *15*, 621–623.
[22] O. Grassman, R. B. Neder, A. Putnis, P. Löbmann, *Am. Mineral.* **2003**, *88*, 647–652.
[23] B. Judat, M. Kind, *J. Colloid Interface Sci.* **2004**, *269*, 341–353.
[24] T. Vossmeyer, G. Reck, L. Katsikas, E. Haupt, B. Schulz, H. Weller, *Science* **1995**, *267*, 1476–1479.
[25] E. V. Shevchenko, D. V. Talapin, A. L. Rogach, A. Kornowski, M. Haase, H. Weller, *J. Am. Chem. Soc.* **2002**, *124*, 11480–11485.
[26] S. Wohlrab, *PhD thesis* Potsdam **2004**.
[27] T. Kato, A. Sugawara, N. Hosoda, *Adv. Mater.* **2002**, *14*, 869–877.
[28] H. Cölfen, *Curr. Opin. Colloid Interface Sci.* **2003**, *8*, 23–31.

[29] A. M. Belcher, X. H. Wu, R. J. Christensen, P. K. Hansma, G. D. Stucky, D. E. Morse, *Nature* **1996**, *381*, 56–58.
[30] M. Fritz, A. M. Belcher, M. Radmacher, D. A. Walters, P. K. Hansma, G. D. Stucky, D. E. Morse, S. Mann, *Nature* **1994**, *371*, 49–51.
[31] A. Berman, L. Addadi, S. Weiner, *Nature* **1988**, *331*, 546–548.
[32] J. Aizenberg, J. Hanson, T. F. Koetzle, S. Weiner, L. Addadi, *J. Am. Chem. Soc.* **1997**, *119*, 881–886.
[33] S. Albeck, S. Weiner, L. Addadi, *Chem. Eur. J.* **1996**, *2*, 278–284.
[34] L. Addadi, S. Weiner, *Proc. Natl. Acad. Sci. USA* **1985**, *82*, 4110–4114.
[35] L. B. Gower, D. J. Odom, *J. Cryst. Growth* **2000**, *210*, 719–734.
[36] G. Falini, M. Gazzano, A. Ripamonti, *J. Cryst. Growth* **1994**, *137*, 577–584.
[37] A. Taubert, G. Glasser, D. Palms, *Langmuir* **2002**, *18*, 4488–4494.
[38] S. Mann, D. D. Archibald, J. M. Didymus, T. Douglas, B. R. Heywood, F. C. Meldrum, N. J. Reeves, *Science* **1993**, *261*, 1286–1292.
[39] E. K. Giannimaras, P. G. Koutsoukos, *Langmuir* **1988**, *4*, 855–861.
[40] C. A. Orme, A. Noy, A. Wierzbicki, M. T. McBride, M. Grantham, H. H. Teng, P. M. Dove, J. J. DeYoreo, *Nature* **2001**, *411*, 775–779.
[41] F. Manoli, S. Koutsopoulos, E. Dalas, *J. Cryst. Growth* **1997**, *182*, 116–124.
[42] E. Dalas, P. G. Koutsoukos, *Langmuir* **1988**, *4*, 907–910.
[43] S. Mann, B. R. Heywood, S. Rajam, J. D. Birchall, *Nature* **1988**, *334*, 692–695.
[44] J. Lahiri, G. F. Xu, D. M. Dabbs, N. Yao, I. A. Aksay, J. T. Groves, *J. Am. Chem. Soc.* **1997**, *119*, 5449–5450.
[45] P. J. J. A. Buijnsters, J. J. J. M. Donners, S. J. Hill, B. R. Heywood, R. J. M. Nolte, B. Zwanenburg, N. A. J. M. Sommerdijk, *Langmuir* **2001**, *17*, 3623–3628.
[46] J. Kuther, G. Nelles, R. Seshadri, M. Schaub, H. J. Butt, W. Tremel, *Chem. Eur. J.* **1998**, *4*, 1834–1842.
[47] J. Aizenberg, A. J. Black, G. M. Whitesides, *Nature* **1999**, *398*, 495–498.
[48] T. X. Wang, H. Cölfen, M. Antonietti, *J. Am. Chem. Soc.* **2005**, *127*, 3246–3247.
[49] H. Schnablegger, O. Glatter, *Appl. Optics*, **1991**, *30*, 4889–4896.
[50] N. Gehrke, H. Cölfen, N. Pinna, M. Antonietti, N. Nassif, *Cryst. Growth Des.* **2005**, *5*, 1317–1319.
[51] C. G. Sinn, R. Dimova, M. Antonietti, *Macromolecules* **2004**, *37*, 3444–3450.
[52] H. Cölfen, A. Völkel; *Progr. Colloid Polym. Sci.* **2006**, *131*, 126–128.
[53] J. Bolze, B. Peng, N. Dingenouts, P. Panine, T. Narayanan, M. Ballauff, *Langmuir* **2002**, *18*, 8364–8369.
[54] L. A. Estroff, L. Addadi, S. Weiner, A. D. Hamilton, *Org. Biomol. Chem.* **2004**, *2*, 137–141.
[55] O. Grassmann, P. Löbmann, *Chem. Eur. J.* **2003**, *9*, 1310–1316.
[56] a) R. Fortey, "Crystal eyes - vision of trilobites" *Natural History* **2000**, 10; b) R. Fortey, *Trilobite - Eyewitness to Evolution*, Harper Collins, Canada **2000**.
[57] R. Kniep, S. Busch, *Angew. Chem.* **1996**, *108*, 2788–2791; *Angew. Chem. Int. Ed. Engl.* **1996**, *35*, 2624–2626.
[58] S. Busch, H. Dolhaine, A. DuChesne, S. Heinz, O. Hochrein, F. Laeri, O. Podebrad, U. Vietze, T. Weiland, R. Kniep, *Eur. J. Inorg. Chem.* **1999**, *10*, 1643–1653.
[59] W. Shan, B. Wang, Y.-H. Zhang, B.-Y. Wu, Y. Tang, *Chem. Lett.* **2004**, *33*, 1248–1249.
[60] A. A. Marino, R. O. Becker, *Calcif. Tissue Res.* **1974**, *14*, 327–331.
[61] H. Cölfen, L. M. Qi, *Chem. Eur. J.* **2001**, *7*, 106–116.
[62] S. H. Yu, H. Cölfen, M. Antonietti, *J. Phys. Chem. B* **2003**, *107*, 7396–7405.
[63] L. M. Qi, H. Cölfen, M. Antonietti, M. Li, J. D. Hopwood, A. J. Ashley, S. Mann, *Chem. Eur. J.* **2001**, *7*, 3526–3532.
[64] S. H. Yu, H. Cölfen, M. Antonietti, *Chem. Eur. J.* **2002**, *8*, 2937–2945.
[65] S. H. Yu, M. Antonietti, H. Cölfen, J. Hartmann, *Nano. Lett.* **2003**, *3*, 379–382.
[66] S. H. Yu, M. Antonietti, H. Cölfen, M. Giersig, *Angew. Chem.* **2002**, *114*, 2462–2466; *Angew. Chem. Int. Ed.* **2002**, *41*, 2356–2360.

Received: August 22, 2005
Revised: March 14, 2006